Orbital Velocities Induced by Surface Waves

LYNN K. SHAY

Division of Meteorology and Physical Oceanography, Rosenstiel School of Marine and Atmospheric Science, University of Miami, Miami, Florida

EDWARD J. WALSH*

NASA Goddard Space Flight Center, Wallops Flight Facility, Wallops Island, Virginia

PEN CHEN ZHANG

Division of Meteorology and Physical Oceanography, Rosenstiel School of Marine and Atmospheric Science, University of Miami, Miami, Florida

(Manuscript received 16 August 1993, in final form 16 August 1993)

ABSTRACT

During the third intensive observational period of the Surface Wave Dynamics Experiment (SWADE), an aircraft-based experiment was conducted on 5 March 1991 by deploying slow-fall airborne expendable current profilers (AXCPs) and airborne expendable bathythermographs (AXBTs) during a scanning radar altimeter (SRA) flight on the NASA NP-3A research aircraft. As the Gulf Stream moved into the SWADE domain in late February, maximum upper-layer currents of 1.98 m s^{-1} were observed in the core of the baroclinic jet where the vertical current shears were $O(10^{-2}\ s^{-1})$. The SRA concurrently measured the sea surface topography, which was transformed into two-dimensional directional wave spectra at 5–6-km intervals along the flight tracks. The wave spectra indicated a local wave field with wavelengths of 40–60 m propagating southward between 120° and 180°, and a northward-moving swell field from 300° to 70° associated with significant wave heights of 2–4 m.

As the AXCP descended through the upper ocean, the profiler sensed orbital velocity amplitudes of 0.2–0.5 m s^{-1} due to low-frequency surface waves. These orbital velocities were isolated by fitting the observed current profiles to the three-layer model based on a monochromatic surface wave, including the steady and current shear terms within each layer. The depth-integrated differences between the observed and modeled velocity profiles were typically less than 3 cm s^{-1}. For 17 of the 21 AXCP drop sites, the rms orbital velocity amplitudes, estimated by integrating the wave spectra over direction and frequency, were correlated at a level of 0.61 with those derived from the current profiles. The direction of wave propagation inferred from the AXCP-derived orbital velocities was in the same direction observed by the SRA. These mean wave directions were highly correlated (0.87) and differed only by about 5°.

1. Introduction

A jointly sponsored Office of Naval Research (ONR) and National Aeronautics and Space Administration (NASA) Surface Wave Dynamics Experiment (SWADE) (Weller et al. 1990) was conducted offshore of the Delmarva Peninsula along the United States east coast from October 1990 through March 1991. The objective of this multi-institutional, international field program was to understand the evolving dynamics of the surface wave field and to assess the effect of waves on air–sea fluxes. During the month of February 1991, the Gulf Stream (GS) moved inshore and a warm-core ring (WCR) began to coalesce with the north wall of the GS in early March. Previous studies (Joyce 1985; Evans et al. 1985) have shown that these upper-ocean features frequently occur in the SWADE experimental domain, which have a direct impact on the evolving surface wave spectra and air–sea fluxes (Bane and Osgood 1989).

During the third intensive observational period (IOP) of SWADE, slow-fall airborne expendable current profilers (AXCPs) and airborne expendable bathythermographs (AXBTs) were deployed during a scanning radar altimeter (SRA) (Walsh et al. 1985) flight from the NASA NP-3A research aircraft on 5 March 1991. The AXCPs and AXBTs provided a high-resolution, three-dimensional snapshot of the ocean

* Currently on assignment at NOAA Environmental Technology Laboratory, Boulder, Colorado.

Corresponding author address: Dr. Lynn Keith Shay, Division of Meteorology and Physical Oceanography, Rosenstiel School of Marine and Atmospheric Science, 4600 Rickenbacker Causeway, Miami, FL 33149-1098.

current and temperature structure in the vicinity of the GS. The SRA directly measured the sea surface topography that was transformed into the directional wave spectra beneath the aircraft using a two-dimensional fast Fourier transform (FFT). Additional measurements of the velocity and temperature structure were acquired from the RV *Frederic G. Creed* in the WCR using an acoustic Doppler current profiler (ADCP) and expendable bathythermographs (XBTs). Thus, a unique dataset consisting of upper-ocean observations and remotely sensed wave spectra were acquired in a sheared baroclinic zone for the first time.

Since the development of the AXCP (the airborne version of the shipboard XCP), an important scientific issue has been the measurement of the surface wave–induced orbital velocities as the profiler descends through the mixed layer, and inferring the direction of propagation of the low-frequency surface wave field. Using a combination of fast-fall (4.5 m s^{-1}) and slow-fall (2.2 m s^{-1}) profilers, Sanford et al. (1987) developed a three-layer model to isolate the surface wave signals sensed by the AXCPs deployed in Hurricanes Norbert and Josephine. These waves had surface current amplitudes of 1–2 m s^{-1} that exponentially decayed with depth. As a result of these experiments and the requirement to improve the resolution of the upper-ocean orbital velocities, Osse et al. (1988) developed a two-speed AXCP version that descended at a rate of less than 1 m s^{-1} in the upper 200 m during the Ocean Storms Experiment (D'Asaro et al. 1990). These two-speed AXCPs sensed several realizations of surface waves in the upper 200 m, thereby improving the resolution of the orbital velocities. Although the surface wave–induced orbital velocities have not been independently verified by surface wave measurements, the observational evidence indicates that the large amplitude wavelike excursions from the mean and the sheared mixed-layer velocities are due to low-frequency surface waves, not measurement error or electronic noise.

The objective here is to relate the surface wave orbital velocities and the direction of wave propagation observed from the AXCPs to those derived from the simultaneous two-dimensional directional wave spectra measurements from the SRA. The surface wave contributions to the current profilers are isolated using the three-layer approach of Sanford et al. (1987) based upon a monochromatic wave associated with the swell. In the low-frequency part of the spectra, the spectra are integrated over direction and frequency to determine an rms orbital velocity amplitude at each AXCP drop site (Tynan 1986). The mean directions of wave propagation from the SRA are compared to those inferred from the AXCP data. The experimental sampling strategy, observations, and data quality are briefly described in section 2. The observed current structure and the two-dimensional wave spectra at selected points are given in section 3. The orbital velocity amplitudes and directions of wave propagation derived from the three-layer model are compared to those determined from the SRA in section 4, and concluding statements are given in section 5.

2. Data description

a. Experimental design

Based on Advanced Very High Resolution Radiometer (AVHRR) images, the SRA/AXCP research flight was conducted on 5 March 1991 (third IOP) starting at 1650 UTC and ending at 2300 UTC. A total of 23 slow-fall AXCPs and 10 AXBTs were deployed at 30-km intervals in a starlike pattern skewed toward the warm side of the GS (Fig. 1). Of the 33 AXCPs and AXBTs deployed on the research flight, oceanographic data were telemetered to the aircraft from 30 of the probes for a success rate of 90% (Table 1). Four of the AXCPs only provided data in the upper 70–90 m (instead of 250 m) and a few profiles contained noisy temperatures. The last AXCP was deployed within 2 km of the RV *Frederic G. Creed* and an ADCP current profile in the WCR located toward the northwest of the GS. After removal of the depth-averaged flow from the ADCP profile, the comparison to the closest AXCP revealed correlations of 0.87 and 0.96 between the horizontal velocity components with rms errors of 2.3 and 2.7 cm s^{-1} (Shay 1993).

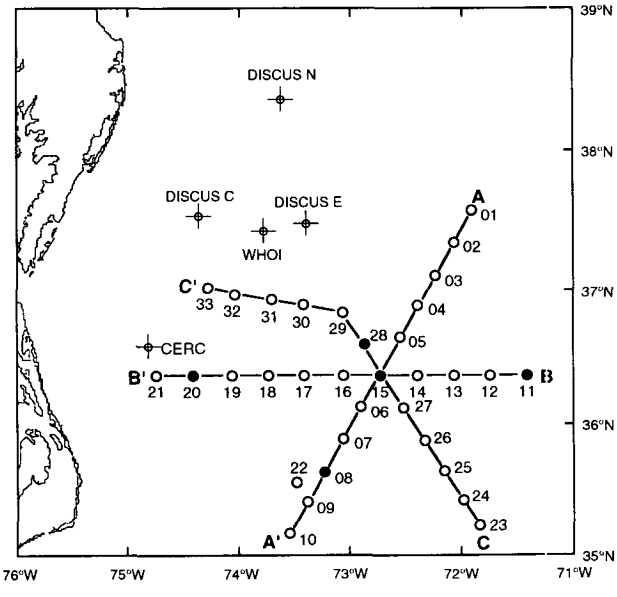

FIG. 1. AXCP and AXBT deployments in a starlike pattern along three flight tracks of the NASA NP-3A at 30-km intervals along sections *AA'*, *BB'*, and *CC'*. The shaded circles represent selected wave spectra from the SRA current profiles at various points relative to the Gulf Stream that are used in detailed comparisons, and the numbers correspond to the drop sites referred to in the tables. The SWADE surface moorings are depicted by circles with plus signs.

TABLE 1. Times and positions of AXCP (CP) and AXBTs (BT) deployed on the 5 March 1991 from the NASA NP-3A SRA research flight during SWADE. The comments are coded as 1—RF/AF failures (no data); 2—variable rotation rate; 3—noisy $T(z)$ signal; and depth of last data point for short profiles.

Drop number	Time UTC	Latitude (N)	Longitude (W)	Type	Comments
01	1755	37°34.70'N	71°53.60'W	CP	1
02	1813	37°20.50'N	72°06.06'W	BT	
03	1817	36°05.30'N	72°17.00'W	CP	70 m
04	1824	36°51.20'N	72°26.60'W	BT	
05	1827	36°37.40'N	72°36.20'W	CP	
06	1837	36°07.40'N	72°56.70'W	CP	90 m
07	1842	35°53.10'N	73°06.80'W	CP	1
08	1847	35°37.20'N	73°14.50'W	CP	2
09	1852	35°24.30'N	73°24.20'W	CP	
10	1859	35°07.80'N	73°34.40'W	BT	
11	2002	36°21.80'N	71°25.30'W	CP	
12	2007	36°22.00'N	71°44.80'W	BT	
13	2012	36°22.40'N	72°05.20'W	CP	75 m
14	2017	36°22.70'N	72°25.00'W	CP	
15	2022	36°22.70'N	72°44.80'W	CP	
16	2027	36°22.70'N	73°05.10'W	CP	
17	2032	36°22.50'N	73°25.10'W	CP	85 m
18	2037	36°22.10'N	73°44.80'W	CP	
19	2042	36°21.70'N	74°05.20'W	BT	
20	2047	36°21.10'N	74°25.20'W	CP	
21	2057	36°22.20'N	74°42.70'W	BT	
22	2120	35°32.10'N	73°29.70'W	BT	
23	2148	35°07.40'N	71°54.90'W	BT	
24	2153	35°20.30'N	72°03.80'W	CP	
25	2201	35°34.80'N	72°14.10'W	BT	
26	2204	35°49.80'N	72°24.90'W	CP	3
27	2209	36°04.10'N	72°35.30'W	CP	
28	2219	36°31.90'N	72°55.70'W	CP	
29	2224	36°44.40'N	73°07.50'W	CP	3
30	2230	36°48.90'N	73°33.20'W	CP	3
31	2235	36°52.60'N	73°53.00'W	CP	
32	2241	36°57.30'N	74°06.90'W	CP	
33	2244	37°07.20'N	74°23.80'W	BT	1

The optimal aircraft altitude for AXCP deployments is 1500 m above the ocean's surface. However, the aircraft flew beneath the cloud deck at 640 m at indicated airspeeds (IAS) of about 92 m s^{-1} to deploy the AXCPs. This IAS was within the envelope found in the Ocean Storms (D'Asaro et al. 1990), Hurricane Gilbert (Shay et al. 1992), and the Northeast Pacific Ocean Experiments (Shay 1992) to achieve 80%–90% success rates of the AXCPs. The altitude and speed of the aircraft were also optimal for the SRA to acquire high-resolution measurements of the sea surface topography.

b. *Atmospheric conditions*

On the morning of 4 March, maximum winds of 15 m s^{-1} were observed at discus east (E), and the winds at discus north (N) and central (C) exceeded 10 m s^{-1} in the same direction as a low pressure area located over Pennsylvania moved toward the northeast (not shown). By the next day, this cell was centered along the Maine coast associated with southerly winds of 7–13 m s^{-1} that extended into the SWADE domain. As the storm continued to move toward the northeast, a high pressure ridge dominated the weather during the afternoon of 5 March. The surface wind speeds decreased to 3–7 m s^{-1} when the winds changed from a southerly to a northwesterly direction. The significant wave heights (SWH) ranged from 2 to 4 m for peak wave periods of 10–12 s due to low-frequency swell.

c. *AXCP*

The AXCP is the airborne version of the XCP that senses the ocean's relative velocity by measuring the motionally induced voltage difference between two electrodes spaced 5 cm apart (Sanford et al. 1982). The XCP accurately samples the baroclinic current structure relative to an unknown, but depth-independent velocity with rms errors of 1–2 cm s^{-1} over 2–3-m depth intervals. Although the depth-independent component is not resolved by the XCP, the barotropic flow is about 0.1–0.2 m s^{-1} in the GS (Halkin and Rossby 1985) or at most 5%–10% of the total baroclinic signal of 2 m s^{-1}. The AXCPs deployed in SWADE were modified to fall slowly at a rate of 2.2 m s^{-1} to resolve the upper-ocean currents and temperatures (to 250 m), and the orbital velocities of the low-frequency surface wave components.

d. *SRA*

The NASA/Goddard Space Flight Center (GSFC) has a long history of measuring the directional wave spectrum using the surface contour radar (SCR) (Walsh et al. 1985, 1989). The SRA, a mode of the 36-GHz GSFC multimode airborne radar altimeter (Parsons and Walsh 1989), has replaced the SCR as the instrument of choice in the measurement of sea surface directional wave spectra. Both the SCR and SRA scan a narrow beam across the aircraft ground track, but the SRA has higher power and a wider swath. It measures the slant range to 64 points (versus 51 for the SCR) evenly spaced across the swath (at 8-m intervals for a 640-m altitude), converts them to surface elevations, and as the aircraft advances at a nominal speed of 100 m s^{-1}, displays the false-color-coded topography on a monitor in real time. This grid of surface topography represents a snapshot of the wave field with along-track spacing of 12–13 m between points. These data over an along-track distance of 5–6 km and a cross-track swath of about 520 m are transformed into directional wave spectra by a two-dimensional FFT.

The two-dimensional FFT of the wave topography produces an encounter spectrum in wavenumber space. This encounter spectrum must be Doppler corrected because of the finite time it takes the aircraft to acquire the data. The Doppler corrections and the transformation into the frequency domain are derived by as-

suming a linear dispersion relationship, and ignoring any effect of ocean current (Walsh et al. 1985). Doppler shifts in frequency (or wavenumber) by the ocean currents (maximum of 2 m s^{-1}) are at least a second-order term in this correction compared to the speed of the aircraft (about 100 m s^{-1}).

3. Observations

a. Velocity structure

The velocity profiles along section *CC'* in Fig. 1 indicated the most pronounced horizontal variability in the upper-ocean structure (Fig. 2). The weak currents at sites 24 and 27 contained oscillations in the vertical structure possibly due to vertically propagating near-inertial motions trapped on the Sargasso Sea side of the GS (Kunze 1985); however, these components cannot be resolved because only one AXCP flight was made. The currents started to increase at site 26, and there was a maximum near-surface current of about 1.5 m s^{-1} at sites 15 and 28. The maximum observed current in the core of the GS was about 1.98 m s^{-1} along section *BB'* (see Fig. 1) at drop site 17. Notice that the current structure was not vertically homogenous even within the core of the GS because the wave-like excursions were due to the presence of surface wave–induced currents. At site 29, there was a current reversal due to the juxtaposition of a WCR along the north wall of the GS, which is consistent with the AVHRR image on 7 March 1991. The remaining current profiles were deployed in the WCR, where the RV *Frederic G. Creed* acquired current and temperature profiles (C. Flagg 1991, personal communication). The AXCP- and ADCP-derived currents were directed toward the northwest just on the periphery of the WCR, which indicates an anticyclonic rotation of the currents (Joyce 1985).

b. Directional wave spectra

The directional wave spectra (Fig. 3) from four AXCP drop sites, west (20), within (15), east (11), and south (8) of the GS illustrate the spatial variability of the surface waves propagating into a sheared baroclinic current. In Fig. 3a, the spectra observed west of the Gulf Stream at 36.4°N, 74.4°W (site 20) indicated a bimodal wave system with 150-m-wavelength swell propagating toward 335° and a 50-m-wavelength system propagating toward 170°. The SWH in this region was about 2.2 m. The short-wavelength system propagated more southerly than the local wind would suggest. This deviation may have been caused by the Delaware Bay since waves emanating from its mouth during offshore wind conditions tended to dominate the nearshore wave field (Walsh et al. 1983). Note that 170° is the approximate direction from the Delaware Bay mouth to the position of site 20.

The second spectrum (Fig. 3b) was observed just outside the core of the GS at 36.5°N, 72.8°W (sites 15/28) where the SWH was about 3.1 m and the near-surface currents were 1–1.5 m s^{-1} (discussed in section 4a). Here the 150-m-wavelength swell system half-power width spanned from north to 60°, but at the quarter-power level the spectrum was spread from 300° to 70°. The energy density in the 330° direction was reduced to 70% of that in the spectra in Fig. 3a. At site 20, Cape Hatteras would block off swell propagating toward the northeast, so the presence of such swell at drop sites 15 and 28 was not unreasonable. However, at this position Cape Hatteras would also tend to block swell from propagating toward 60°, and its presence may have been due to wave–current interactions. The short-wavelength system contained more angular and frequency dispersion than at site 20 due in part to the interaction with the WCR indicated by the ADCP and AXCP profiles.

At site 11 (36.4°N, 71.5°W), the SWH of 3.8 m was considerably higher than at the other two sites. However, the noise level of the spectra (Fig. 3c) was also higher because of contamination by the aircraft motion induced by atmospheric turbulence. The spectral peak of the 150-m swell system propagated toward

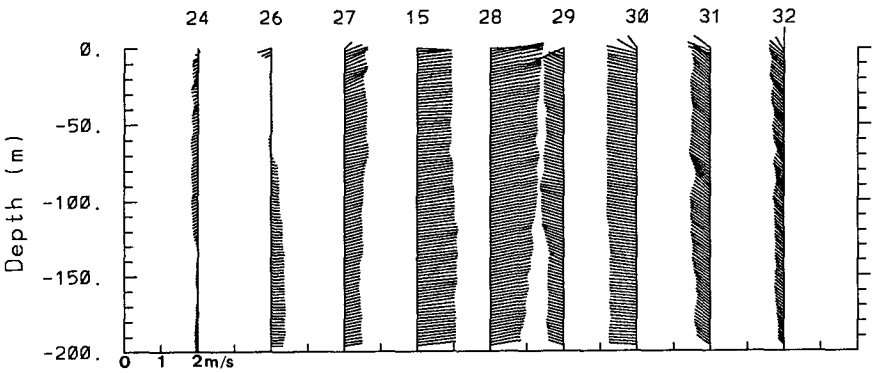

FIG. 2. Current vectors (m s^{-1}) from the AXCPs deployed along section *CC'* in Fig. 1. Each successive velocity profile is offset by 2 m s^{-1}, and the convention for the current is that a current toward the north and east is positive.

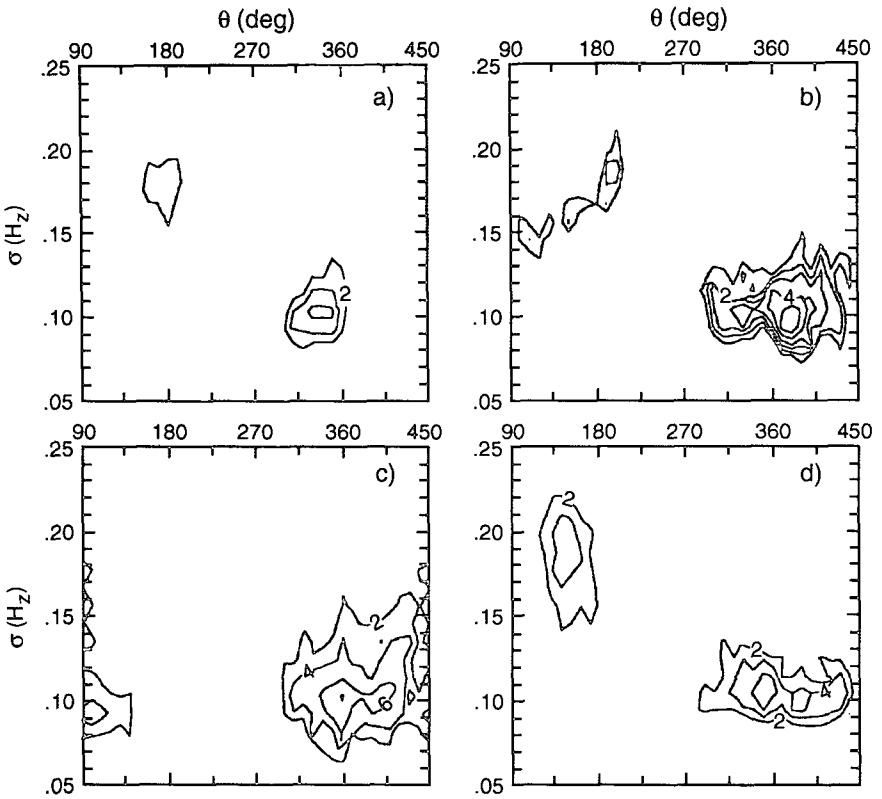

FIG. 3. Selected two-dimensional directional wave spectra from the SRA in absolute variance density using a 1.5-dB contour interval with the lowest contour being 0.01 m^2 (Hz deg)$^{-1}$ at drop sites (a) 20, (b) 15/28, (c) 11, and (d) 08 depicted in Fig. 1.

the north, but the half-power width was spread from about 330° to 60° and the quarter-power width range of 270° to 90°.

Near the southern boundary of the GS at site 8, the 50-m-wavelength system propagated toward 140°, whereas the 150-m-wavelength swell propagation direction was spread from about 280° to 70° with peaks at 355° and 40° (Fig. 3d). The current structure was weak, having amplitudes of 0.1 m s^{-1}, indicating that the AXCP was deployed near the center of the anticyclonically rotating current shear zone, as suggested by AVHRR imagery (not shown).

4. Surface wave–induced orbital velocities

a. Three-layer model

The slow-fall profilers allow a separation of the orbital velocities induced by the surface waves through the mixed layer. For a 10-s wave (λ = 156 m), two or three realizations of the low-frequency surface wave orbital velocities were detected by the slow-fall profilers for typical mixed layer depths of 50–60 m (note that $\sigma^2 = kg$ is the linear deep-water dispersion relation where k is the horizontal wavenumber and g is acceleration of gravity). Sanford et al. (1987) developed a three-layer model for a monochromatic surface wave of the form

$$v_m = e^{kz}\left[C\cos\left(\sigma\frac{z}{W}\right) + S\sin\left(\sigma\frac{z}{W}\right)\right] + V_i^s\left[\left(z - \frac{Z_{i-1} + Z_i}{2}\right)\right] + \bar{V}_i + v_r, \quad (1)$$

where C and S are the amplitude coefficients of the surface wave, W is the fall rate of the profiler, V_i^s represents the shear component, $\bar{V}_i$ is the vertically averaged velocity in ith layer, Z_i is the depth of layer i, z is the actual depth, and v_r is the residual current. A similar expression holds for the u component with additional constraints prescribed in the three-layer model to ensure continuity between layers. The three-layer model fit to the observed velocity profiles at each site using a nonlinear least-squares technique (Marquardt 1963) optimizes the fit by varying σ from 0.07 to 0.14 Hz. These frequencies are within the limits of the low-frequency swell observed in directional wave spectra at each site (Fig. 3).

The three-layer model fit to the observed current profiles indicated energetic orbital velocities induced

by the low-frequency surface wave components starting at z_o, the depth where the electronic noise decreased to less than 0.10 m s^{-1} (Table 2). This value defines the difference between the observed and modeled profiles due to the presence of surface waves in nonstorm deployments compared to about 0.15 m s^{-1} during strong atmospheric forcing events (Sanford et al. 1987). The largest surface wave–induced velocity derived from the fit was 0.73 m s^{-1} at site 11 where the SWH was about 3.8 m. However, more typical values were 0.2 to 0.5 m s^{-1}. Maximum currents in the upper layer exceeded 1 m s^{-1} at sites 5, 28, 16, and 17, where the maximum near-surface current exceeded 1.98 m s^{-1}. These values were within the range of 1.5–2 m s^{-1}, and similar to the Pegasus current profiles across 73°W (Halkin and Rossby 1985). Even at depths of 100–200 m, the currents ranged between 1.3 and 1.7 m s^{-1} within the core of the GS. The upper-layer vertical current shear was largest at site 17 with a value of 2×10^{-2} s^{-1}. Similar orders of magnitude in the vertical current shears at sites 9, 11, and 29 may be due in part to the shallow depth of the upper layer for these profiles.

Given observed SWH of 2–4 m, the surface wave–induced orbital velocities of 0.2–0.5 m s^{-1} were within the range predicted from theory and evident in the normalized velocity profiles (Fig. 4). The surface wave activity in the observed current profiles at site 15 was considerably less than at the other profile sites, and the model fit at site 20 was overestimated (underestimated) in the upper (lower) 50 m. Since the model assumed

TABLE 2. Coefficients from fits with the three-layer model and the AXCP profiles in the upper 200 m where z_o is the start depth of the fit; T is the period of the surface wave with coefficients of C and S; and $Z_{1,2,3}$, $V_{1,2,3}$, and $V^s_{1,2,3}$ represent the layer depths, the layer-averaged currents, and the current gradients in each layer, respectively.

Drop number	T (s)	C (cm s^{-1})	S (cm s^{-1})	z_o (m)	V_1 (cm s^{-1})	V^s_1 (10^{-2} s^{-1})	Z_1 (m)	V_2 (cm s^{-1})	V^s_2 (10^{-2} s^{-1})	Z_2 (m)	V_3 (cm s^{-1})	V^s_3 (10^{-2} s^{-1})	Z_3 (m)
03*u*	15.4	−1.6	−3.5	−8	58	−0.10	−36	61	−0.08	−50	61	0.09	−70
03*v*	10.3	−34.6	9.2	−8	−29	−0.24	−36	−26	0.11	−50	−28	0.19	−70
05*u*	8.5	8.5	11.3	−8	121	0.15	−65	102	0.96	−95	85	0.04	−200
05*v*	13.7	−8.2	7.4	−8	−20	0.05	−65	−20	−0.08	−95	−13	−0.11	−200
06*u*	7.9	−33.2	−22.1	−2	60	0.95	−20	48	0.13	−65	50	−0.42	−88
06*v*	10.8	9.6	−11.8	−2	8	0.24	−20	13	−0.33	−65	21	0.02	−88
08*u*	9.1	−14.4	−0.6	−4	−7	−0.09	−35	13	−0.90	−75	25	0.09	−200
08*v*	10.3	8.9	52.0	−4	17	−0.16	−35	12	0.38	−75	10	−0.09	−200
09*u*	11.5	−15.9	−4.7	−2	−5	−1.46	−20	20	−1.42	−35	31	−0.01	−200
09*v*	8.9	−28.5	6.3	−2	−3	−0.58	−20	−5	1.08	−35	−5	−0.09	−200
11*u*	12.0	−16.6	26.3	−2	5	−0.56	−50	13	0.20	−110	13	−0.14	−200
11*v*	9.7	−70.4	21.7	−2	20	1.06	−50	−3	−0.13	−110	4	−0.07	−200
13*u*	8.9	−25.8	9.4	0	61	0.20	−40	54	0.23	−60	53	−0.16	−72
13*v*	10.8	17.6	7.6	0	−6	0.33	−40	−13	0.06	−60	−3	−1.37	−72
14*u*	8.3	−22.8	−34.4	−4	76	0.03	−60	80	−0.39	−85	88	−0.06	−200
14*v*	9.4	−29.2	17.1	−4	2	0.11	−60	9	−0.77	−85	10	0.14	−200
15*u*	10.9	−6.1	2.1	−4	92	0.08	−65	95	−0.59	−85	103	−0.04	−200
15*v*	11.0	−36.1	18.1	−4	14	0.15	−65	19	−1.02	−85	25	0.08	−200
16*u*	8.2	−18.5	−3.2	−4	143	0.30	−65	140	−0.26	−115	145	0.03	−200
16*v*	8.8	−15.8	26.0	−4	45	0.09	−65	50	−0.29	−115	47	0.24	−200
17*u*	13.2	4.7	−14.0	0	194	2.05	−20	175	−0.13	−35	158	0.78	−82
17*v*	9.3	−40.2	−4.3	0	40	−1.83	−20	45	1.84	−35	32	−0.04	−82
18*u*	10.7	17.5	3.7	−4	52	0.14	−95	49	−0.30	−115	41	0.25	−200
18*v*	10.7	−25.6	2.0	−4	19	0.03	−95	15	0.25	−115	7	0.12	−200
20*u*	11.2	9.1	−4.3	−2	−5	0.02	−65	−2	−0.35	−85	5	−0.06	−200
20*v*	8.5	17.5	−1.4	−2	4	0.03	−65	−1	0.45	−85	1	−0.11	−200
24*u*	10.2	23.0	−8.6	−6	−13	0.11	−65	−11	−0.20	−125	−4	−0.02	−200
24*v*	10.1	9.5	18.9	−6	−16	−0.12	−65	−16	0.12	−125	−24	0.12	−200
26*u*	9.4	9.3	−31.0	−2	59	−0.10	−65	55	0.36	−105	45	0.04	−200
26*v*	11.2	−2.3	−8.2	−2	39	0.28	−65	29	0.03	−105	22	0.15	−200
27*u*	8.9	−2.0	−13.5	−6	−1	0.06	−60	9	−1.15	−80	30	−0.17	−200
27*v*	10.7	−7.4	−21.8	−6	6	0.12	−60	0	0.18	−80	0	−0.02	−200
28*u*	8.9	4.7	−2.4	−2	135	0.42	−45	128	−0.07	−95	106	0.44	−200
28*v*	10.6	−16.0	21.9	−2	55	0.20	−45	54	−0.15	−95	43	0.29	−200
29*u*	11.4	3.7	10.5	−12	−60	−1.32	−20	−51	0.14	−80	−47	−0.15	−200
29*v*	11.5	7.3	12.6	−12	52	1.34	−20	37	0.06	−80	32	0.06	−200
30*u*	9.9	2.6	21.6	−4	−80	−0.09	−20	−79	0.01	−80	−75	−0.07	−200
30*v*	11.1	14.2	−0.7	−4	40	0.58	−20	34	0.01	−80	22	0.20	−200
31*u*	12.5	−4.2	6.9	−6	−49	0.08	−60	−52	0.05	−75	−45	−0.12	−200
31*v*	12.0	4.9	25.0	−6	80	0.10	−60	80	−0.35	−75	69	0.22	−200
32*u*	12.5	−6.8	−1.0	−2	−30	−0.17	−95	−24	0.15	−120	−21	−0.12	−200
32*v*	10.3	38.7	3.0	−2	63	0.18	−95	51	0.34	−120	40	0.15	−200

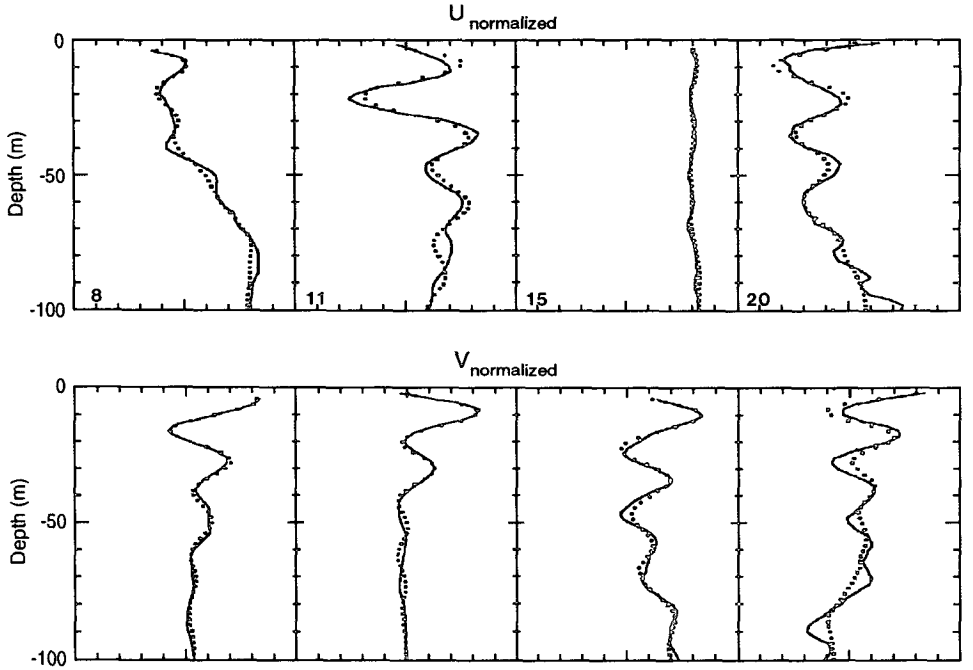

FIG. 4. Observed (solid) and modeled (dotted) u-component (upper panel) and v-component (lower panel) profiles for the three-layer model based on a single wave in the upper 100 m for the selected locations in Figs. 1 and 3. The observed and modeled profiles were normalized with values of 0.34, 0.26, 1.01, and 0.12 m s^{-1} and 0.60, 0.89, 0.47, and 0.19 m s^{-1} for the u and v components at sites 08, 11, 15, and 20, respectively.

a monochromatic surface wave propagating in one direction and these sites were subjected to the more complex surface wave fields, the velocity profiles contain more frequency and directional components that have to be quantitatively compared to the wave spectral data.

b. *Orbital velocity spectra*

The analysis combines the wave spectra data from 17 of the 21 current profiles for times when the positions of the AXCP profiles and the SRA spectra were less than 2 km apart, which is within the resolving capability of the SRA. The orbital velocity spectra were estimated by transforming the directional wave spectra and integrating over direction (Fig. 5) (Tynan 1986). The most apparent feature in the velocity spectra is the bimodal distribution except at site 8. The largest peaks occurred at 0.18 Hz, or an approximate period of 6 s for sites 11, 15, and 20. The secondary spectral peak was at about 0.09–0.11 Hz, associated with the low-frequency swell that directly affects the AXCP velocity profiles. There was a pronounced difference in the spectral peak levels, from 2.5 m^2 s^{-1} at site 8 south of the GS to values exceeding 6.5 m^2 s^{-1} at site 11 and 5.2 m^2 s^{-1} at site 15. At site 20, there was a twofold increase in the orbital velocity spectra from the swell to the higher frequencies. These differences in the spectral peaks at the low and high frequencies correlate well with spatial variations associated with the GS currents (Huang et al. 1972; Phillips 1977).

The rms orbital velocity amplitudes and mean wave directions were determined from the directional wave spectra (Fig. 6). These amplitudes were estimated by integrating the orbital velocity spectra (from 270° to 90°) over frequency from 0.04 to 0.17 Hz, which delineates the primary and secondary peaks in the wave spectra. At $z = z_o$, the scatter of the orbital velocity amplitudes ranged between 0.2 and 0.5 m s^{-1} with a correlation coefficient of 0.61 m s^{-1}. For an rms difference of about 3 cm s^{-1}, a large fraction of the scatter may be due to sampling variability as expected from instantaneous AXCP measurements over 50 s to reach a depth of minimal influence of the low-frequency swell by virtue of the e-folding scale in Eq. (1). The standard deviation between the SRA- and AXCP-derived amplitudes was about 0.11 m s^{-1}, which is consistent with previous studies for surface wave contamination of the velocity signals from AXCPs. The largest disagreement occurred at site 11 where the surface wave–induced current amplitude was 0.73 m s^{-1} compared to 0.45 m s^{-1} from the wave spectra. Over the remaining ensemble, the results are consistent with the findings of Tynan (1986), who modeled the orbital velocities observed from current meter mooring data acquired during the Long Term Upper Ocean Study (Briscoe and Weller 1984).

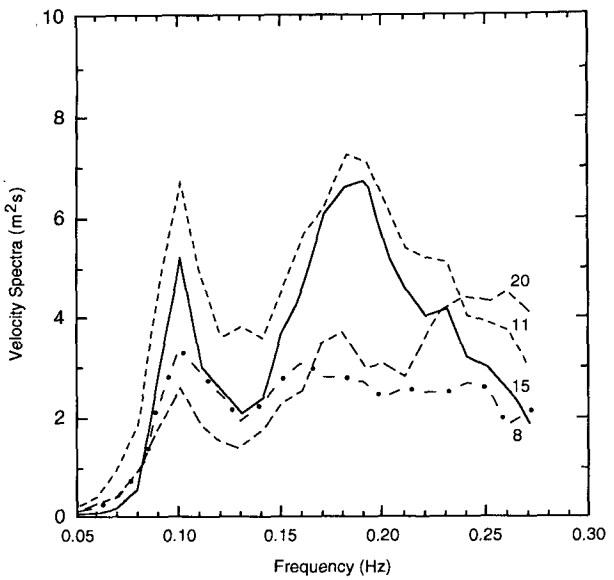

FIG. 5. Orbital velocity spectra ($m^2 s^{-1}$) derived from the 2D directional wave spectra in Fig. 3 and integrating over direction for the drop sites 8, 11, 15, and 20. The abscissa represents the frequency (Hz).

The wave spectra indicated that the primary and secondary peaks were in the direction of 300°–340° and 20°–70° (Fig. 6b). These directions are reflected in the scatter of the AXCP-derived directions of wave propagation and the corresponding wave spectral data. The correlation coefficient of 0.87 was significant with a mean directional difference of about 5° after removing the 180° ambiguity from the wave directions derived from the AXCP data because of the phase of the wave group. That is, at any instant in time, the superposition of surface waves results in a modulation of the wave group based on linear dynamics (Phillips 1977). And, depending on the exact drop position relative to this interaction within the wave group, the AXCP would sense the dominant wave (and its phase) within the packet at that instant in time, not necessarily the most energetic wave in the swell region of the entire spectra.

5. Conclusions

The combined SRA–AXCP research flight was successful in simultaneously measuring the wave fields and current and temperature structure in the Gulf Stream. For the first time, the observed wave and current fields over an approximate 200-km domain yielded extensive information concerning the spatial evolution of the directional wave spectra in a sheared baroclinic current regime. Given the large near-surface currents of about 2 m s^{-1}, and consistent upper-ocean structure patterns with the AVHRR, the AXCPs resolved the synoptic-scale baroclinic structure as in hurricane (Sanford et al. 1987; Shay et al. 1992), Ocean Storms (D'Asaro et al. 1990), and the Northeast Pacific Subarctic Front (Shay 1992) experiments. One of the interesting results was that the velocity structure from the AXCPs showed that the WCR was rejoining the GS as seen in the velocity section and the AVHRR imagery.

The orbital velocities observed by the AXCPs are not electronic noise from the sensor, but represent a physical phenomenon associated with surface waves (Sanford et al. 1987). A nonlinear least-squares technique minimized the residual variance between the modeled and observed current profiles, as in the Hurricane Gilbert profiles, by determining the optimal frequency of the dominant wave in the swell region of the spectra (Shay et al. 1992). Not only was the three-layer model effective in isolating the dominant surface wave–induced velocity in the current profiles, but the

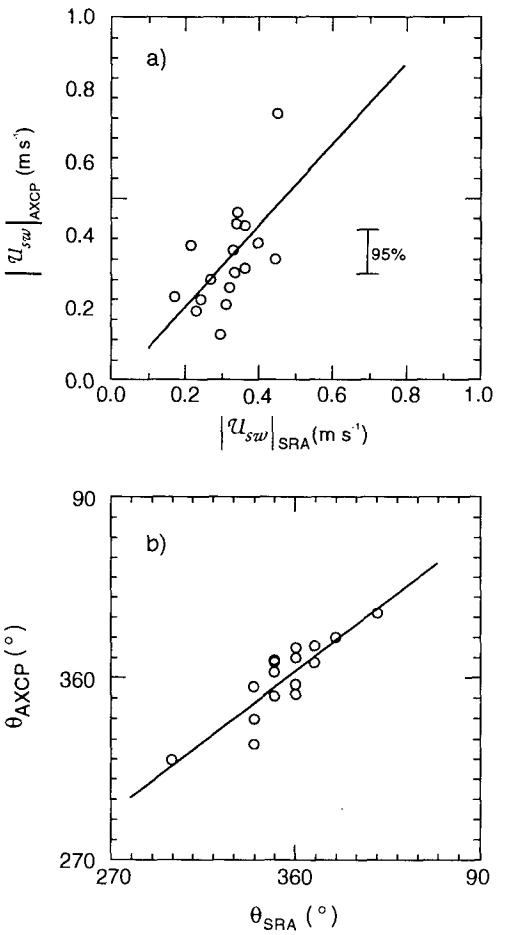

FIG. 6. Scatterplot of (a) rms orbital velocity amplitudes (m s^{-1}) and (b) mean direction of wave propagation (°) based on observed wave spectra (abscissa) and the AXCP current profiles (ordinate). The regression curves (solid) represent the optimal fits between the two measurements with correlations of 0.61 and 0.87 for the amplitudes and directions of wave propagation. The 95% confidence limits are given for the orbital velocity amplitudes based on a Student's t-test of the mean differences (Bendat and Piersol 1971).

rms amplitudes and the mean direction of surface wave propagation agreed well with those observed in the SRA wave spectra. The correlation coefficient of the orbital velocity amplitudes between the two measurements was 0.61, whereas the mean directional differences between the AXCP fits and the SCR data were about 5° with a correlation coefficient of 0.87. Thus, in the absence of directional wave spectral observations from aircraft or buoys, the three-layer model fits to the observed velocity profiles can be used to infer the direction of the propagation of the dominant swell components over the experimental domain.

In future experiments, the phase information between the various wave components should be archived during the FFTs of the sea surface topography for the purpose of performing multiple-wave fits with the three-layer model to the AXCP data based upon linear wave dynamics (Forristall 1982). These data would be particularly useful in storm deployments using the two-speed AXCPs (Osse et al. 1988) when the wind stress excites various wave components. Given a continuum of low-frequency surface waves, a multiwave formulation may resolve more of the observed orbital velocity signals in the AXCP than with a single wave. However, based upon these results, it is encouraging that there is good agreement between the two independent measuring devices of the orbital velocity amplitudes and directions of wave propagation.

Acknowledgments. This research was supported by the Office of Naval Research under Contract N00014-91-J1042 and the Earth Science and Applications Division of NASA Headquarters. The authors extend their appreciation to Tom Sanford and John Dunlap of the Applied Physics Laboratory at the University of Washington for processing the slow-fall AXCP signals. Peter Black of NOAA's Hurricane Research Division provided the HP workstation and the Sippican Mark 10 receiver for the research flight. Don Hines and Wayne Wright of the WFF provided guidance in the installation of the AXCP data acquisition system on the NASA NP-3A, and Pete Bradfield (WFF) orchestrated the multiple-flight missions during SWADE. The authors would also like to thank members of the Scientific Steering Group of SWADE for their guidance in planning the 5 March research flights. Charlie Flagg provided the ADCP data acquired from the RV *Frederic G. Creed.* Hans Graber, George Forristall, and Owen Phillips made comments on earlier versions of the manuscript and technical report. Jean Carpenter redrafted the graphics, and Gay Ingram revised the manuscript based on the editing of Christy Sweet at the NOAA WPL.

REFERENCES

Bane, J. M., and K. E. Osgood, 1989: Winter-time air-sea interaction processes across the Gulf Stream. *J. Geophys. Res.*, **94**, 10 755–10 772.

Bendat, J. S., and A. G. Piersol, 1971: *Random Data: Analysis and Measurement Procedures.* Wiley-Interscience, 407 pp.

Briscoe, M. G., and R. A. Weller, 1984: Preliminary results from the long-term upper ocean study (LOTUS). *Dyn. Atmos. Oceans,* **8**, 243–265.

D'Asaro, E. A., T. B. Sanford, R. X. Drever, M. O. Morehead, and G. L. Welsh, 1990: Air-expendable current profiling during the Ocean Storms Experiment. Tech. Rep. APL-UW TR 8916, 66 pp. [Available from Applied Physics Laboratory, University of Washington, Seattle, WA 98105.]

Evans, R. H., K. S. Baker, O. B. Brown, and R. C. Smith, 1985: Chronology of warm-core ring 82B. *J. Geophys. Res.*, **90**, 8803–8811.

Forristall, G. Z., 1982: Kinematics of directionally spread waves. *Proc. Directional Wave Spectra Applications,* Berkeley, CA, Amer. Soc. Civil Eng., 129–146.

Halkin, D., and T. Rossby, 1985: The structure and transport of the Gulf Stream at 73°W. *J. Phys. Oceanogr.*, **15**, 1439–1452.

Huang, N. E., D. T. Chen, C. C. Tung, and J. R. Smith, 1972: Interactions between steady non-uniform currents and gravity waves with applications for current measurements. *J. Phys. Oceanogr.*, **2**, 420–431.

Joyce, T. M., 1985: Gulf Stream warm core rings collection: An introduction. *J. Geophys. Res.*, **90**, 8801–8802.

Kunze, E., 1985: Near-inertial wave propagation in geostrophic shear. *J. Phys. Oceanogr.*, **15**, 544–565.

Marquardt, D., 1963: An algorithm for least squares estimation of nonlinear parameters. *J. Soc. Ind. Appl. Math.*, **11**, 431–441.

Osse, T. J., R. G. Drever, and T. B. Sanford, 1988: The design and operation of the slowfall AXCP. Tech. Rep. APL-UW 8110, 41 pp. [Available from Applied Physics Lab., University of Washington, Seattle, WA 98105.]

Parsons, C., and E. J. Walsh, 1989: Off-nadir radar altimetry. *IEEE Trans. Geosci. Remote Sens.*, **27**, 215–224.

Phillips, O. M., 1977: *The Dynamics of the Upper Ocean.* 2d ed. Cambridge University Press, 336 pp.

Sanford, T. B., R. G. Drever, J. H. Dunlap, and E. A. D'Asaro, 1982: Design, operation and performance of an expendable temperature and velocity profiler (XTVP). Tech. Rep. APL-UW 8110, 83 pp. [Available from Applied Physics Lab., University of Washington, Seattle, WA 98105.]

——, P. G. Black, J. Haustein, J. W. Fenney, G. Z. Forristall, and J. F. Price, 1987: Ocean response to hurricanes. Part I: Observations. *J. Phys. Oceanogr.*, **17**, 2065–2083.

Shay, L. K., 1992: Airborne expendable current profiling in the subarctic front during the Northeast Pacific Ocean Experiment. RSMAS Tech. Rep. 92-003, 99 pp. [Available from Rosenstiel School of Marine and Atmospheric Science, University of Miami, Miami, FL 33149.]

——, 1993: Airborne expendable current profiling in the Surface Wave Dynamics Experiment. RSMAS Tech. Rep. 93-001, 46 pp. [Available from Rosenstiel School of Marine and Atmospheric Science, University of Miami, Miami, FL 33149.]

——, P. G. Black, A. J. Mariano, J. D. Hawkins, and R. L. Elsberry, 1992: Upper ocean response to hurricane Gilbert. *J. Geophys. Res.*, **97**, 20 227–20 248.

Tynan, C. T., 1986: A comparison of modeled and observed wave orbital velocities at the surface and near the surface during the Long Term Upper Ocean Study (LOTUS). Informal Tech. Rep., 23 pp. [Available from Woods Hole Oceanographic Institute, Woods Hole, MA 02543.]

Walsh, E. J., D. W. Hancock III, D. E. Hines, R. N. Swift, and J. F. Scott, 1985: Directional wave spectra measured with the surface contour radar. *J. Phys. Oceanogr.*, **15**, 566–592.

——, ——, ——, ——, and ——, 1989: An observation of the directional wave spectrum evolution from shoreline to fully developed sea. *J. Phys. Oceanogr.*, **19**, 670–690.

Weller, R. A., M. A. Donelan, M. G. Briscoe, and N. E. Huang, 1990: Riding the crest: A tale of two wave experiments. *Bull. Amer. Meteor. Soc.*, **72**, 163–183.